

Observation of non-Hermitian dislocation bound states and dislocation skin effects

Jia-Xin Zhong,¹ Bitan Roy,^{2,*} and Yun Jing^{1,†}

¹Graduate Program in Acoustics, The Pennsylvania State University, University Park, PA 16802, USA

²Department of Physics, Lehigh University, Bethlehem, Pennsylvania 18015, USA

The confluence of Non-Hermitian (NH) topology and crystal defects has culminated significant interest, yet its experimental exploration has been limited due to the challenges involved in design and measurements. Here, we showcase experimental observation of NH dislocation bound states (NHDS) and the dislocation-induced NH skin effect in two-dimensional acoustic NH Chern lattices. By embedding edge dislocations in such acoustic lattices and implementing precision-controlled hopping and onsite gain/loss via active meta-atoms, we reveal robust defect-bound states localized at dislocation cores within the line gap of the complex energy spectrum. These NHDS survive against moderate NH perturbations but gradually delocalize and merge with the bulk (skin) states as the system arrives at the shore of fostering exceptional points in the Brillouin zone under periodic (open) boundary conditions. Furthermore, our experiments demonstrate that the dislocation core can feature weak NH skin effects when its direction is perpendicular to the Burgers vector in periodic systems. Our findings pave an experimental pathway for probing NH topology via lattice defects and open new avenues for defect-engineered topological devices.

Introduction. Crystalline defects, such as dislocations [1–14] and disclinations [15–18], play pivotal roles in the identification of topological crystals in nature and topological metamaterials in laboratory [19–22]. In Hermitian topological systems, these defects can host robust bound states, protected by a combination of crystalline symmetry and topological invariant as dictated by the bulk-defect correspondence, analogous to the celebrated bulk-boundary correspondence. The emergence of non-Hermitian (NH) physics, where gain/loss and non-reciprocity play significant roles, introduces radical departures from conventional Hermitian behavior [23–33]. For instance, NH systems often exhibit phenomena such as the NH skin effect (NHSE), in which a macroscopic number of eigenstates accumulate at the boundaries, obscuring the traditional bulk-boundary signature [34–42]. These effects necessitate alternative strategies for detecting and characterizing NH topological phases.

Recent theoretical advances have identified crystalline defects as robust local topological probes in NH systems, potentially overcoming the limitations imposed by the NHSE [38, 43]. In particular, Panigrahi *et al.* theoretically showed that dislocations in a NH Chern insulator can host robust in-gap bound states, protected by pseudo-particle-hole symmetry, whose spatial localization and stability are governed by both NH parameters and the defect geometry [38]. Moreover, an interplay between the dislocation and NHSE can give rise to a dislocation-induced NHSE (D-NHSE), manifesting a typical skin accumulation around the defect core under periodic boundary conditions (PBCs) [36–38]. However, experimental observation of these fascinating phenomena has remained far from reality due to the requirement for delicate defect engineering combined with precision-

controlled NH perturbations, along with the inherent difficulty in probing complex energy spectrum [44–49].

In this work, we circumvent these challenges by embedding edge dislocations into a two-dimensional (2D) acoustic lattice implemented using a coupled acoustic cavity system (CACS) and by introducing controlled NH perturbations via active meta-atoms [35, 49–54]. By employing a recently proposed Green’s function approach [49], we directly measure the complex-valued energy spectrum along with both left and right eigenstates of the system. Our experimental platform thereby enables the observation of NH dislocation states (NHDS) emerging within the line gap of the complex energy spectrum, as well as the D-NHSE. We further demonstrate that while

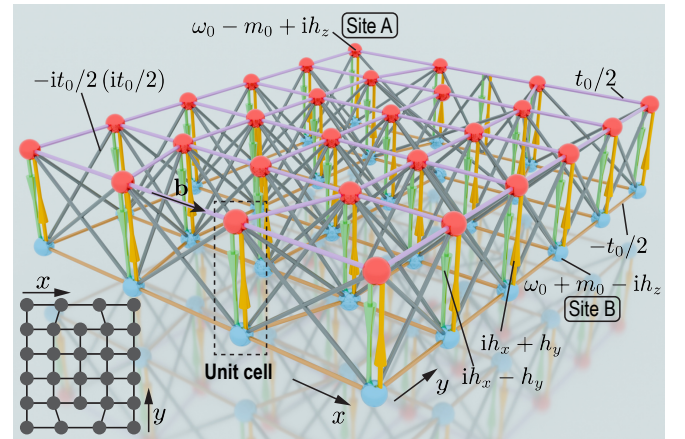


FIG. 1. Schematic implementation of a NH Chern insulator [Eq. (1)] in the presence of an edge dislocation-antidislocation pair with Burgers vectors $\mathbf{b} = \pm \mathbf{e}_x$. Each unit cell consists of two sites labeled by A (red ball) and B (blue ball). Solid bars of the same color represent the reciprocal hopping amplitudes of equal strength, and those with arrows indicate nonreciprocal hopping amplitudes. Bottom left inset shows the top view, where circles represent unit cells.

* bitan.roy@lehigh.edu

† yqj5201@psu.edu

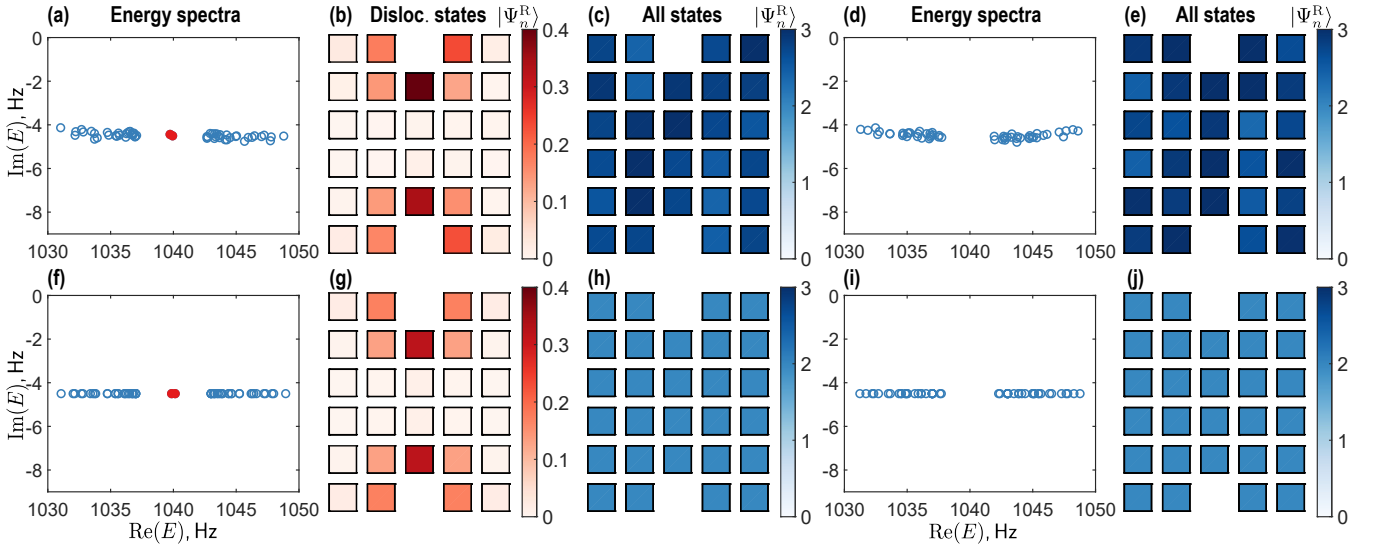


FIG. 2. Hermitian ($\mathbf{h} = 0$) acoustic Chern insulators in the presence of an edge dislocation-antidislocation pair under periodic boundary conditions (PBCs), showing (a)-(e) experimental observations and (f)-(j) theoretical computations. Energy spectrum [(a) and (f)], amplitude distributions of right eigenstates of the dislocation modes, shown by red dots in (a) and (f) within unit cells [(b) and (g)] and all the states [(c) and (h)] in the M phase with $t_0 = -m_0 = 3$ Hz. Energy spectra [(d) and (i)] and amplitude distributions of all the right eigenstates [(e) and (j)] in the Γ phase with $t_0 = m_0 = 3$ Hz.

the NHDS persist under moderate NH perturbations, they lose support in the system with the appearance of the exceptional points (EPs) therein. As this threshold is approached from the weak NH perturbation side, NHDS gradually delocalize and merge into the bulk (skin) states under periodic (open) boundary conditions; a process coinciding with the closure of the NH band gap, in quantitative agreement with theoretical predictions. Overall, our work bridges the gap between NH band topology and defect physics, establishing crystal defects as universal tools for probing NH topological matter.

Model and design. We consider a 2D NH Chern insulator whose Bloch Hamiltonian is expressed as [27, 38, 55]

$$H_{\text{NH}}(\mathbf{k}) = H_{\text{H}}(\mathbf{k}) + i\boldsymbol{\sigma} \cdot \mathbf{h} = \boldsymbol{\sigma} \cdot [\mathbf{d}(\mathbf{k}) + i\mathbf{h}], \quad (1)$$

where $\mathbf{d}(\mathbf{k}) = (t_0 \sin k_x, t_0 \sin k_y, t_0[\cos k_x + \cos k_y] - m_0)$, the vector Pauli matrix $\boldsymbol{\sigma} = (\sigma_x, \sigma_y, \sigma_z)$, $i = \sqrt{-1}$, and we set the lattice spacing $a = 1$. The Hermitian part is denoted as $H_{\text{H}}(\mathbf{k}) = \boldsymbol{\sigma} \cdot \mathbf{d}(\mathbf{k})$ and the anti-Hermitian operator is $i\boldsymbol{\sigma} \cdot \mathbf{h}$ with $\mathbf{h} = (h_x, h_y, h_z) \in \mathbb{R}^3$. The phase diagram of this model is detailed in the Supplemental Material (SM) [56]. In this model, an edge dislocation-antidislocation pair is introduced by removing two unit cells located at opposite ends along the y -direction and subsequently reconnecting the sites along the x -direction, see Fig. 1. As a result, any closed path encircling the dislocation core lacks a translation by the Burgers vector $\mathbf{b} = \pm \mathbf{e}_x$.

We implement this NH Chern insulator using a CACS. In our design, each acoustic cavity, which supports a dipole resonant mode at the frequency $\omega_0 = 1040 \text{ Hz} - 4.5i \text{ Hz}$, serves as a lattice site. See SM for further details [56]. Here, the imaginary part of ω_0 represents the

intrinsic background loss. As illustrated in Fig. 1, each unit cell comprises two coupled cavities labeled by A and B. The intra-unit-cell coupling between these two cavities is rendered by the nonreciprocal NH perturbations, yielding asymmetric hopping amplitudes $ih_x - h_y$ and $ih_x + h_y$, while the inter-unit-cell hopping amplitudes are reciprocal. Both the nonreciprocal and reciprocal couplings are realized via detector-source pairs (i.e., microphone-loudspeaker systems) [49, 54]. For instance, the hopping from site 1 to site 2 is achieved by detecting the acoustic pressure at site 1 and then driving the loudspeaker at site 2 accordingly. In addition, to accurately tune the staggered onsite potentials $\pm m_0$ and the distributed gain/loss corresponding to $\pm ih_z$, we establish a feedback loop within each cavity; a microphone detects the local acoustic pressure and the corresponding loudspeaker modulates the response. The magnitude and phase of each microphone-loudspeaker pair are meticulously adjusted to realize the desired hopping parameters and onsite potentials.

Measurements. Probing the wave dynamics in NH lattices poses unique challenges due to the presence of complex-valued eigenenergies, which manifest as complex poles in the Green's functions of the system. Conventional single-site excitation techniques, relying on the real or simple complex frequency excitations cannot selectively target these poles [44–49, 54]. To overcome this limitation, we employ a Green's function-based measurement method [49]. In our experiments, a source (loudspeaker) is sequentially activated at every site, depicted in Fig. 1, and the resulting frequency responses are simultaneously captured by an array of microphones. This procedure yields the full Green's function $G(\omega)$ as a

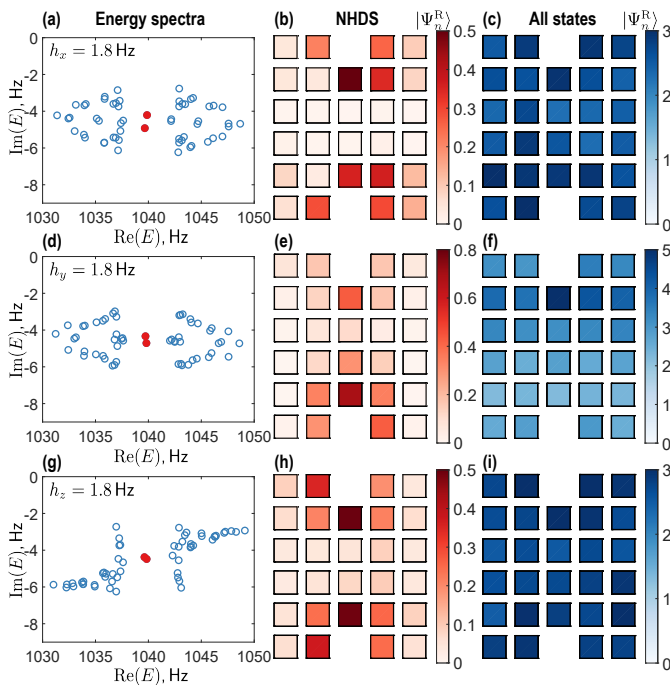


FIG. 3. Experimental observation on an acoustic Chern lattice with an edge dislocation-antidislocation pair under PBCs and *moderate* NH perturbations for $t_0 = -m_0 = 3$ Hz. (a) Complex energy spectrum for $\mathbf{h} = (1.8 \text{ Hz}, 0, 0)$. (b) Total amplitude of two right eigenvectors of NHDS marked by red dots in (a). (c) Total amplitude of all the right eigenstates from (a). Panels (d)-(f) [(g)-(i)] are analogous to (a)-(c), respectively, but with $\mathbf{h} = (0, 1.8 \text{ Hz}, 0)$ [$\mathbf{h} = (0, 0, 1.8 \text{ Hz})$].

function of the excitation frequency ω , from which the complex-valued eigenenergies and corresponding right and left eigenstates are extracted by leveraging the established correspondence with the real-space Hamiltonian.

Parameter space. To ensure a comprehensive observation, we choose four distinct values of each NH perturbation in experiments; $h_y = h_z = 0$ and $h_x/t_0 = 0.3, 0.6, 0.9, 1.1$, with analogous values for h_y and h_z . We also include the Hermitian case ($\mathbf{h} = 0$), resulting in a total of 13 configurations. For each configuration, experiments were performed under open boundary conditions (OBCs) and PBCs in two distinct phases; the M phase with $t_0 = -m_0 = 3$ Hz and $\mathbf{K} = (\pi, \pi)$, and the Γ phase with $t_0 = m_0 = 3$ Hz and $\mathbf{K} = (0, 0)$. Here, \mathbf{K} is the band inversion momentum. In total, 52 cases were explored, with all experimentally measured complex-valued energy spectra, left and right eigenstates, and corresponding theoretical predictions detailed in the SM [56].

Observations of NHDS and D-NHSE. We begin our investigation by examining the dislocation bound states in the Hermitian limit ($\mathbf{h} = 0$). Figure 2 displays the experimental results for both the M and Γ phases. The measured complex energy spectra and corresponding right eigenstates exhibit excellent agreement with theoretical predictions. Namely, only the M phase hosts mid-gap dislocation states as $\mathbf{K} \cdot \mathbf{b} = \pm\pi$ (nontrivial) around the

defect core therein, whereas the Γ phase is devoid of such defect modes for which $\mathbf{K} \cdot \mathbf{b} = 0$ (trivial) [1, 4, 5]. The right eigenstate weight at the n -th unit cell is defined as $\Psi_n^R = \sum_m (|\psi_{m,A}^R|^2 + |\psi_{m,B}^R|^2)$, where the index m sums over either the two states near zero energy corresponding to the dislocation states [Figs. 2(b) and 2(g)] or all states [Figs. 2(c), 2(e), 2(h), and 2(j)]. In this notation, $\psi_{m,\xi}^R$ denotes the right eigenstate for the m th state at site ξ within the unit cell, with $\xi = A, B$. Notably, PBCs are imposed in Fig. 2 to suppress midgap edge states, thereby enhancing the visibility of dislocation states. SM shows corresponding results under OBCs [56].

As illustrated in Fig. 2(a), two distinct midgap states are clearly observed in the M phase, with their spatial profiles localized at the dislocation cores, see Fig. 2(b). The dislocation modes are separated from the bulk states, see Fig. 2(c). By contrast, the Γ phase reveals only bulk eigenstates, with no midgap energies detected, see Figs. 2(d) and 2(e). These findings are consistent with the theoretical prediction that a Hermitian Chern insulator hosting a dislocation supports zero-energy states only in the M phase, where the first Chern number $C = -1$ [4], see also Figs. 2(f)-2(j).

Upon introducing moderate NH perturbations, the energy spectra become considerably more intricate, as shown in Fig. 3. See SM for corresponding theoretical predictions [56]. Nevertheless, two NHDS remain pinned near zero-energy within the line gap between 1038 Hz and 1042 Hz (approximately), distinguishing them from the point-gap associated with typical NHSE in other NH lattices [34]. The spatial distribution of the corresponding eigenstates reveals their pronounced dependence on the NH perturbations in the system. Specifically, Fig. 3(b) shows that when only h_x is nonzero, the weight of the right eigenstates is biased along the x -direction, with a greater concentration on the right side ($+x$) of the dislocation cores. This observation is consistent with the fact that this NH perturbation breaks (preserves) the reflection symmetry about y -axis (x -axis). Similarly, Fig. 3(e) depicts that for only a nonzero h_y , the eigenstate weight shifts along the y -direction, with an enhanced intensity near the bottom dislocation core, as this NH perturbation breaks (preserves) the reflection symmetry about x -axis (y -axis). By contrast, when only h_z is nonzero, the intrinsic C_4 symmetry of $H_H(\mathbf{k})$ is preserved, resulting in an approximately symmetric eigenstate distribution along both x and y directions, see Fig. 3(h).

Furthermore, the geometry of dislocations (encoded in the Burgers vector) plays a crucial role in determining the fate of the D-NHSE under PBCs. As shown in Fig. 1, the dislocation core possesses one (two) nearest-neighbor sites in the y (x) direction when the Burgers vector is $\mathbf{b} = \pm\mathbf{e}_x$, thus mimicking the coordination number of a site living on an y directional boundary. Consequently, under PBC, no NHSE is observed for nonzero h_x near the defect core, see Fig. 3(c), while nonzero h_y yields a D-NHSE as shown in Fig. 3(f). However, D-NHSE is relatively *weak* compared to the conventional NHSE ob-

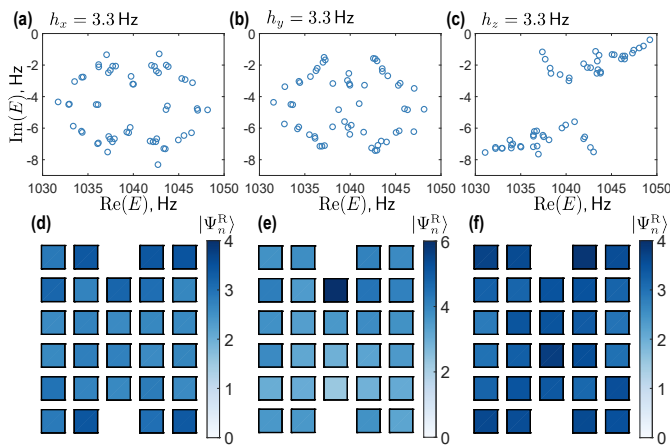


FIG. 4. Similar to Fig. 3, but for *strong* NH perturbations, showing the absence of NHDS. Complex energy spectrum for (a) $\mathbf{h} = (3.3 \text{ Hz}, 0, 0)$ (b) $\mathbf{h} = (0, 3.3 \text{ Hz}, 0)$, and (c) $\mathbf{h} = (0, 0, 3.3 \text{ Hz})$. Corresponding total amplitude of all the right eigenstates are shown in (d), (e), and (f), respectively.

served under OBC at the exterior boundaries of the system. See the SM for a detailed comparison [56]. Notably, when only h_z is finite, no NHSE is observed anywhere in the system, irrespective of the boundary conditions.

Melting of NHDS. As the strength of NH perturbations increases, initially well-localized NHDS gradually spread away from the defect cores. Under PBC, where the conventional NHSE is not supported, the weight of these states is progressively absorbed into the bulk. This trend is observed with different perturbation levels $h_j/t_0 = 0.3, 0.6, 0.9$ for $j = x, y, z$, as detailed in the SM [56]. A similar behavior is found for the left eigenstates. Nonetheless, in the presence of dislocations, the NH Chern insulators with $C = -1$ continues to support topologically robust localized states around the defect cores, which happens for $|h_j| < t_0$ when $|m_0| = t_0$.

For the parameter setting $t_0 = -m_0 = 3 \text{ Hz}$, the EPs, where the real and imaginary parts of the eigenvalues of $H_{\text{NH}}(\mathbf{k})$ vanish, first appear in the Brillouin zone when $h_j = 3 \text{ Hz}$ for $j = x, y, z$. As the system approaches such NH band gap closing, NHDS begin to lose their localization near the defect cores and gradually merge into the bulk states. This melting process is demonstrated in Fig. 4, where the system is placed slightly above the critical NH perturbation $h_j = 3.3 \text{ Hz}$ for $j = x, y, z$, further detailed in the SM. In the strong NH perturbation regime, the NHDS near zero-energy disappear, and only the summed weight of all right eigenstates is presented in Fig. 4(d)-(f), showing that the localized defect states have fully merged into the bulk under PBC. As further corroborated by experiments under OBC (see SM), the NHDS are found to completely merge into the skin modes living at the exterior boundaries of the system. Collectively, Figs. 3, 4, and the SM provide clear evidence for a localization-delocalization phase transition in the NHDS, a phenomenon exclusively observable in NH systems.

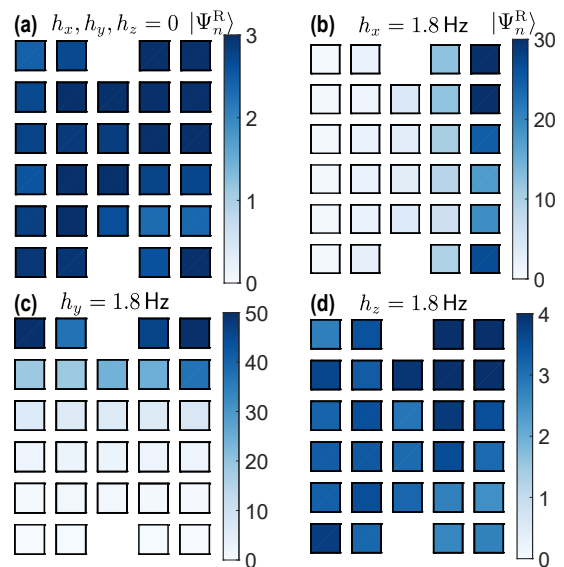


FIG. 5. Experimental observations of the total amplitude of all right eigenstates under OBCs in the M phase with $t_0 = -m_0 = 3 \text{ Hz}$ for (a) $\mathbf{h} = (0, 0, 0)$ (Hermitian limit), (b) $\mathbf{h} = (1.8 \text{ Hz}, 0, 0)$, (c) $\mathbf{h} = (0, 1.8 \text{ Hz}, 0)$, and (d) $\mathbf{h} = (0, 0, 1.8 \text{ Hz})$.

It is noteworthy that Fig. 4(e) illustrates a pronounced D-NHSE in the absence of NHDS for stronger h_y , with a higher right eigenstate weight at the top dislocation core compared to that for a weaker h_y , shown in Fig. 3(f). By contrast, for nonzero h_x and h_z , the D-NHSE is either absent (likelihood) or much weaker, as shown in Figs. 4(d) and 4(f), respectively. Therefore, our experimental observation clearly demonstrates D-NHSE that is distinct from the conventional point-gap supported NHSE under OBC [34] and depends on the relative orientation of the Burgers vector and the directionality of the NHSE.

Observations under OBC. Under OBC, the spatial distribution of the summed weight of all right eigenstates reveals valuable insights. For a Hermitian insulator and a NH one with nonzero h_z , such a weight extends uniformly throughout the entire lattice, as shown in Figs. 5(a) and 5(d), respectively, confirming the absence of any NHSE therein. However, with the NH perturbations h_x and h_y a clear signature of NHSE emerges, with the right wavefunctions localizing toward the positive x and y boundaries, respectively, shown in Figs. 5(b) and 5(c). This anisotropic behavior stems from the broken reflection and inversion symmetries by the NH perturbations h_x and h_y . With the emergence of NHSE along the edges, the dislocation cores themselves do not exhibit a pronounced NHSE under OBC for nonzero h_x and h_y . By contrast, when the Burgers vector is perpendicular to the direction of the NHSE observed under OBC, a D-NHSE becomes visible under PBC, as shown in Fig. 4(e).

Summary and discussions. To summarize, our experiments provide conclusive evidences for NHDS and D-NHSE in a 2D acoustic Chern insulator. In the Hermitian limit, dislocations host zero-energy states in the M phase,

consistent with the bulk-defect correspondence [1, 4, 5]. Under moderate NH perturbations, these states persist within the line gap. As the perturbation strength increases, we observe a localization-delocalization transition for NHDS as they gradually spread and merge with bulk states under PBCs when the system approaches the shore of hosting EPs in the Brillouin zone [38]. By contrast, the D-NHSE appears for any arbitrary strength of NH perturbations, when the direction of the conventional

NHSE is orthogonal to the Burgers vector. Our results not only bridge the gap between NH band topology and defect physics but also establish crystalline defects as a universal tool for probing NH topological matter.

Acknowledgments. Y.J. thanks the support of startup funds from Pennsylvania State University and NSF awards 2039463, 195122, and 2401236. B.R. was supported by NSF CAREER Grant No. DMR-2238679.

-
- [1] Y. Ran, Y. Zhang, and A. Vishwanath, One-dimensional topologically protected modes in topological insulators with lattice dislocations, *Nat. Phys.* **5**, 298 (2009).
- [2] J. C. Y. Teo and C. L. Kane, Topological defects and gapless modes in insulators and superconductors, *Phys. Rev. B* **82**, 115120 (2010).
- [3] D. Asahi and N. Nagaosa, Topological indices, defects, and Majorana fermions in chiral superconductors, *Phys. Rev. B* **86**, 100504 (2012).
- [4] V. Juričić, A. Mesaros, R.-J. Slager, and J. Zaanen, Universal Probes of Two-Dimensional Topological Insulators: Dislocation and π Flux, *Phys. Rev. Lett.* **108**, 106403 (2012).
- [5] R.-J. Slager, A. Mesaros, V. Juričić, and J. Zaanen, The space group classification of topological band-insulators, *Nat. Phys.* **9**, 98 (2012).
- [6] R.-J. Slager, A. Mesaros, V. Juričić, and J. Zaanen, Interplay between electronic topology and crystal symmetry: Dislocation-line modes in topological band insulators, *Phys. Rev. B* **90**, 241403 (2014).
- [7] T. L. Hughes, H. Yao, and X.-L. Qi, Majorana zero modes in dislocations of Sr_2RuO_4 , *Phys. Rev. B* **90**, 235123 (2014).
- [8] H. Hamasaki, Y. Tokumoto, and K. Edagawa, Dislocation conduction in Bi-Sb topological insulators, *Appl. Phys. Lett.* **110**, 092105 (2017).
- [9] A. K. Nayak, J. Reiner, R. Queiroz, H. Fu, C. Shekhar, B. Yan, C. Felser, N. Avraham, and H. Beidenkopf, Resolving the topological classification of bismuth with topological defects, *Science Advances* **5**, eaax6996 (2019).
- [10] R. Queiroz, I. C. Fulga, N. Avraham, H. Beidenkopf, and J. Cano, Partial Lattice Defects in Higher-Order Topological Insulators, *Phys. Rev. Lett.* **123**, 266802 (2019).
- [11] B. Roy and V. Juričić, Dislocation as a bulk probe of higher-order topological insulators, *Phys. Rev. Res.* **3**, 033107 (2021).
- [12] T. Nag and B. Roy, Anomalous and normal dislocation modes in Floquet topological insulators, *Commun. Phys.* **4**, 157 (2021).
- [13] S. S. Yamada, T. Li, M. Lin, C. W. Peterson, T. L. Hughes, and G. Bahl, Bound states at partial dislocation defects in multipole higher-order topological insulators, *Nat Commun* **13**, 2035 (2022).
- [14] S. K. Das and B. Roy, Dynamic melting and condensation of topological dislocation modes, *Phys. Rev. B* **108**, 144304 (2023).
- [15] J. C. Y. Teo and T. L. Hughes, Existence of Majorana-Fermion Bound States on Disclinations and the Classification of Topological Crystalline Superconductors in Two Dimensions, *Phys. Rev. Lett.* **111**, 047006 (2013).
- [16] W. A. Benalcazar, J. C. Y. Teo, and T. L. Hughes, Classification of two-dimensional topological crystalline superconductors and Majorana bound states at disclinations, *Phys. Rev. B* **89**, 224503 (2014).
- [17] C. W. Peterson, T. Li, W. Jiang, T. L. Hughes, and G. Bahl, Trapped fractional charges at bulk defects in topological insulators, *Nature* **589**, 376 (2021).
- [18] Y. Liu, S. Leung, F.-F. Li, Z.-K. Lin, X. Tao, Y. Poo, and J.-H. Jiang, Bulk-disclination correspondence in topological crystalline insulators, *Nature* **589**, 381 (2021).
- [19] Z.-K. Lin, Q. Wang, Y. Liu, H. Xue, B. Zhang, Y. Chong, and J.-H. Jiang, Topological phenomena at defects in acoustic, photonic and solid-state lattices, *Nat. Rev. Phys.* , 1 (2023).
- [20] F.-F. Li, H.-X. Wang, Z. Xiong, Q. Lou, P. Chen, R.-X. Wu, Y. Poo, J.-H. Jiang, and S. John, Topological light-trapping on a dislocation, *Nat Commun* **9**, 2462 (2018).
- [21] Q. Wang, Y. Ge, H.-x. Sun, H. Xue, D. Jia, Y.-j. Guan, S.-q. Yuan, B. Zhang, and Y. D. Chong, Vortex states in an acoustic Weyl crystal with a topological lattice defect, *Nat. Commun.* **12**, 3654 (2021).
- [22] H. Xue, D. Jia, Y. Ge, Y.-j. Guan, Q. Wang, S.-q. Yuan, H.-x. Sun, Y. D. Chong, and B. Zhang, Observation of Dislocation-Induced Topological Modes in a Three-Dimensional Acoustic Topological Insulator, *Phys. Rev. Lett.* **127**, 214301 (2021).
- [23] T. E. Lee, Anomalous edge state in a non-Hermitian lattice, *Phys. Rev. Lett.* **116**, 133903 (2016).
- [24] D. Leykam, K. Y. Bliokh, C. Huang, Y. D. Chong, and F. Nori, Edge Modes, Degeneracies, and Topological Numbers in Non-Hermitian Systems, *Phys. Rev. Lett.* **118**, 040401 (2017).
- [25] F. K. Kunst, E. Edvardsson, J. C. Budich, and E. J. Bergholtz, Biorthogonal Bulk-Boundary Correspondence in Non-Hermitian Systems, *Phys. Rev. Lett.* **121**, 026808 (2018).
- [26] E. J. Bergholtz, J. C. Budich, and F. K. Kunst, Exceptional topology of non-Hermitian systems, *Rev. Mod. Phys.* **93**, 015005 (2021).
- [27] K. Kawabata, K. Shiozaki, and M. Ueda, Anomalous helical edge states in a non-Hermitian Chern insulator, *Phys. Rev. B* **98**, 165148 (2018).
- [28] K. Kawabata, K. Shiozaki, M. Ueda, and M. Sato, Symmetry and topology in non-hermitian physics, *Phys. Rev. X* **9**, 041015 (2019).
- [29] C. H. Lee and R. Thomale, Anatomy of skin modes and topology in non-Hermitian systems, *Phys. Rev. B* **99**, 201103 (2019).
- [30] K. Zhang, Z. Yang, and C. Fang, Correspondence between Winding Numbers and Skin Modes in Non-

- Hermitian Systems, *Phys. Rev. Lett.* **125**, 126402 (2020).
- [31] D. S. Borgnia, A. J. Kruchkov, and R.-J. Slager, Non-Hermitian Boundary Modes and Topology, *Phys. Rev. Lett.* **124**, 056802 (2020).
- [32] Y.-X. Xiao and C. T. Chan, Topology in non-Hermitian Chern insulators with skin effect, *Phys. Rev. B* **105**, 075128 (2022).
- [33] J. Bartlett and E. Zhao, Unravelling the edge spectra of non-Hermitian Chern insulators, *Phys. Rev. B* **107**, 035101 (2023).
- [34] S. Yao and Z. Wang, Edge States and Topological Invariants of Non-Hermitian Systems, *Phys. Rev. Lett.* **121**, 086803 (2018).
- [35] L. Zhang, Y. Yang, Y. Ge, Y.-J. Guan, Q. Chen, Q. Yan, F. Chen, R. Xi, Y. Li, D. Jia, S.-Q. Yuan, H.-X. Sun, H. Chen, and B. Zhang, Acoustic non-Hermitian skin effect from twisted winding topology, *Nat. Commun.* **12**, 6297 (2021).
- [36] B. A. Bhargava, I. C. Fulga, J. van den Brink, and A. G. Moghaddam, Non-Hermitian skin effect of dislocations and its topological origin, *Phys. Rev. B* **104**, L241402 (2021).
- [37] F. Schindler and A. Prem, Dislocation non-Hermitian skin effect, *Phys. Rev. B* **104**, L161106 (2021).
- [38] A. Panigrahi, R. Moessner, and B. Roy, Non-Hermitian dislocation modes: Stability and melting across exceptional points, *Phys. Rev. B* **106**, L041302 (2022).
- [39] S. Manna and B. Roy, Inner skin effects on non-Hermitian topological fractals, *Commun. Phys.* **6**, 10 (2023).
- [40] N. Chadha, A. G. Moghaddam, J. van den Brink, and C. Fulga, Real-space topological localizer index to fully characterize the dislocation skin effect, *Phys. Rev. B* **109**, 035425 (2024).
- [41] H. Liu, M. Lu, S. Chai, Z.-Q. Zhang, and H. Jiang, Measurement of the Chern number for non-Hermitian Chern insulators, *Phys. Rev. B* **109**, 155404 (2024).
- [42] V. Kozii and L. Fu, Non-hermitian topological theory of finite-lifetime quasiparticles: Prediction of bulk fermi arc due to exceptional point, *Phys. Rev. B* **109**, 235139 (2024).
- [43] R. Banerjee, S. Mandal, Y. Y. Terh, S. Lin, G.-G. Liu, B. Zhang, and Y. D. Chong, Topological Disclination States and Charge Fractionalization in a Non-Hermitian Lattice, *Phys. Rev. Lett.* **133**, 233804 (2024).
- [44] L. Xiong, Q. Zhang, X. Feng, Y. Leng, M. Pi, S. Tong, and C. Qiu, Tracking intrinsic non-Hermitian skin effects in lossy lattices, *Phys. Rev. B* **110**, L140305 (2024).
- [45] Z. Gu, H. Gao, H. Xue, J. Li, Z. Su, and J. Zhu, Transient non-Hermitian skin effect, *Nat. Commun.* **13**, 7668 (2022).
- [46] H. Gao, W. Zhu, H. Xue, G. Ma, and Z. Su, Controlling acoustic non-Hermitian skin effect via synthetic magnetic fields, *Appl. Phys. Rev.* **11**, 031410 (2024).
- [47] T. Jiang, C. Zhang, R.-Y. Zhang, Y. Yu, Z. Guan, Z. Wei, Z. Wang, X. Cheng, and C. T. Chan, Observation of non-Hermitian boundary induced hybrid skin-topological effect excited by synthetic complex frequencies, *Nat. Commun.* **15**, 10863 (2024).
- [48] J. Huang, K. Ding, J. Hu, and Z. Yang, Complex Frequency Fingerprint (2024), arXiv:2411.12577 [cond-mat].
- [49] J.-X. Zhong, J. Kim, K. Chen, J. Lu, K. Ding, and Y. Jing, Experimentally Probing Non-Hermitian Spectral Transition and Eigenstate Skewness (2025), arXiv:2501.08160 [cond-mat].
- [50] J.-J. Liu, Z.-W. Li, Z.-G. Chen, W. Tang, A. Chen, B. Liang, G. Ma, and J.-C. Cheng, Experimental Realization of Weyl Exceptional Rings in a Synthetic Three-Dimensional Non-Hermitian Phononic Crystal, *Phys. Rev. Lett.* **129**, 084301 (2022).
- [51] Q. Zhang, Y. Li, H. Sun, X. Liu, L. Zhao, X. Feng, X. Fan, and C. Qiu, Observation of acoustic non-Hermitian Bloch braids and associated topological phase transitions, *Phys. Rev. Lett.* **130**, 017201 (2023).
- [52] Z.-X. Chen, Y.-G. Peng, Z.-G. Chen, Y. Liu, P. Chen, X.-F. Zhu, and Y.-Q. Lu, Robust temporal adiabatic passage with perfect frequency conversion between detuned acoustic cavities, *Nat. Commun.* **15**, 1478 (2024).
- [53] L. Zhang, Y. Ge, Y.-j. Guan, F. Chen, N. Han, Q. Chen, Y. Pan, D. Jia, S.-q. Yuan, H.-x. Sun, J. Christensen, H. Chen, and Y. Yang, Nonreciprocal Acoustic Devices with Asymmetric Peierls Phases, *Phys. Rev. Lett.* **133**, 136601 (2024).
- [54] J.-X. Zhong, P. F. De Castro, T. Lu, J. Kim, M. Oudich, J. Ji, L. Shi, K. Chen, J. Lu, Y. Jing, and W. A. Benalcazar, Higher-order skin effect and its observation in an acoustic kagome lattice, *Phys. Rev. B* **111**, 014314 (2025).
- [55] X.-L. Qi, Y.-S. Wu, and S.-C. Zhang, Topological quantization of the spin Hall effect in two-dimensional paramagnetic semiconductors, *Phys. Rev. B* **74**, 085308 (2006).
- [56] See supplemental material for additional experimental results and supporting theoretical analysis.